

# Cryo-EM structure of an activated GPR4–Gs signaling complex

Received: 5 June 2024

Accepted: 3 January 2025

Published online: 11 January 2025

 Check for updates

Yitong Ma<sup>1,6</sup>, Yijie Wang<sup>1,6</sup>, Mengyuan Tang<sup>2,6</sup>, Yuan Weng<sup>1</sup>, Ying Chen<sup>1</sup>, Yueming Xu<sup>1</sup>, Shuxiao An<sup>1</sup>, Yiran Wu<sup>3</sup>, Suwen Zhao<sup>3,4</sup>, Huanhuan Xu<sup>5</sup>, Dali Li<sup>1</sup>, Mingyao Liu<sup>1</sup>, Weiqiang Lu<sup>1</sup>✉, Heng Ru<sup>2</sup>✉ & Gaojie Song<sup>1</sup>✉

G protein-coupled receptor 4 (GPR4) belongs to the subfamily of proton-sensing GPCRs (psGPCRs), which detect pH changes in extracellular environment and regulate diverse physiological responses. GPR4 was found to be overactivated in acidic tumor microenvironment as well as inflammation sites, with a triad of acidic residues within the transmembrane domain identified as crucial for proton sensing. However, the 3D structure remains unknown, and the roles of other conserved residues within psGPCRs are not well understood. Here we report cryo-electron microscopy (cryo-EM) structures of active zebrafish GPR4 at both pH 6.5 and 8.5, each highlighting a distribution of histidine and acidic residues at the extracellular region. Cell-based assays show that these ionizable residues moderately influence the proton-sensing capacity of zebrafish GPR4, compared to the more significant effects of the triad residues. Furthermore, we reveal a cluster of aromatic residues within the orthosteric pocket that may propagate the signaling to the intercellular region via repacking the aromatic patch at the central region. This study provides a framework for future signaling and functional investigation of psGPCRs.

G protein-coupled receptors (GPCRs) represent a diverse group of seven transmembrane proteins constituting the largest superfamily within the human genome and many other genomes. GPCRs play a pivotal role in sensing a wide array of extracellular stimuli, including light, neurotransmitters, hormones, and proteins. Upon stimulation, GPCRs undergo conformational changes, initiating downstream signaling pathways that culminate in specific cellular response<sup>1–3</sup>. Remarkably, ~35% of approved drugs in the pharmaceutical market target GPCRs<sup>4</sup>. Of the 826 GPCRs identified in humans, only three receptors, namely GPR4, GPR65, and GPR68, are characterized as proton-sensing GPCRs (psGPCRs) since they are activated in response to the extracellular acidic environment. Beyond their responsiveness to protons, psGPCRs have previously been implicated in sensing

certain lysolipids<sup>5</sup> and membrane stretching force<sup>6</sup>, albeit with mechanisms that remain to be debated and explored.

psGPCRs have been implicated in several well-documented pH-dependent physiological activities<sup>7</sup>. Local acidity is a typical feature of many pathological processes, including inflammatory, and neurological diseases, and solid tumor<sup>8,9</sup>. Elevated fermentative metabolism and poor perfusion are major causes of local acidity, which has been hypothesized to promote disease progression<sup>10</sup>. Notably, studies have suggested that psGPCRs are highly expressed in tumor cells and the tumor microenvironment (TME)<sup>11–14</sup>. This observation is particularly significant given that the pH in the TME typically registers 0.5–1 unit lower than in normal tissues, primarily attributed to the Warburg effect. This metabolic phenomenon, characterized by increased

<sup>1</sup>Shanghai Frontiers Science Center of Genome Editing and Cell Therapy, Shanghai Key Laboratory of Regulatory Biology, Institute of Biomedical Sciences and School of Life Sciences, East China Normal University, Shanghai, China. <sup>2</sup>Life Sciences Institute, Second Affiliated Hospital of Zhejiang University School of Medicine, Zhejiang Provincial Key Laboratory for Cancer Molecular Cell Biology, Zhejiang University, Hangzhou, Zhejiang, China. <sup>3</sup>Human Institute, ShanghaiTech University, Shanghai, China. <sup>4</sup>School of Life Science and Technology, ShanghaiTech University, Shanghai, China. <sup>5</sup>College of Science, Yunnan Agricultural University, Kunming, China. <sup>6</sup>These authors contributed equally: Yitong Ma, Yijie Wang, Mengyuan Tang. ✉e-mail: [wqlu@bio.ecnu.edu.cn](mailto:wqlu@bio.ecnu.edu.cn); [hengru@zju.edu.cn](mailto:hengru@zju.edu.cn); [gjsong@bio.ecnu.edu.cn](mailto:gjsong@bio.ecnu.edu.cn)

glucose uptake and lactic acid production in rapidly proliferating tumor cells, contributes to the acidification of the extracellular milieu. In addition, it is noteworthy that GPR4 is widely expressed in distinct tissues, including immune, brain, respiratory, and digestive systems, whereas expression of GPR65 and GPR68 seems to be tissue-restricted.

There are several studies that explored the mechanism of psGPCR activation. Early studies implicated a cluster of extracellular histidine residues as primary pH sensors<sup>15–18</sup>, whereas more recent data found that proton-sensing is primarily accomplished by a triad of acidic residues within the transmembrane domain<sup>19</sup>. Interestingly, the phylogenetic analysis suggested that these psGPCRs evolved from GPR132, which lacks one buried acidic residue and is not considered as proton-sensing receptor; on the contrary, no phylogenetic feature can be found for the distributed histidines<sup>19</sup>. Nevertheless, the entire pathway still shows limitations due to the lack of experimental structures. In this study, we report the cryo-electron microscopy (cryo-EM) structures of active GPR4 at both pH 6.5 and 8.5, each coupled to an engineered G<sub>s</sub> protein. These structures, combined with cell-based assays, offer valuable insights into the proton-sensing mechanisms and signal transduction pathways within the psGPCR family.

## Results

### Structure determination

For cryo-EM studies we employed the NanoBiT tethering strategy to facilitate the formation of stable GPR4–G<sub>s</sub> complexes (Supplementary Fig. 1)<sup>20</sup>. To facilitate the binding of a single chain variable fragment (scfv16) (see “Methods”), we modified Gα<sub>s</sub> based on mini-Gα<sub>s</sub>, replacing its αN with the equivalent region from Gα<sub>i</sub><sup>21</sup>. We screened GPR4 species from human, rabbit, and zebrafish using these strategies and found that zebrafish GPR4 (named zGPR4 hereafter) yielded a

homogeneous complex with the engineered G<sub>s</sub> protein. zGPR4 share >60% sequence identity with human GPR4 (hGPR4), with even higher in the G<sub>s</sub> protein-interacting region. Specifically, there is only one residue difference in the intercellular half of the TM5–TM6 region between hGPR4 (S211<sup>CL3</sup>) and zGPR4 (N219<sup>CL3</sup>). Hence, the zGPR4–G<sub>s</sub> complex offers insights into how hGPR4 may recognize its downstream G protein and initiate signaling pathways. We prepared the zGPR4–G<sub>s</sub> complex samples under two conditions, one at pH 6.5 and the other at pH 8.5. Although the basic condition is expected to generate an inactive receptor, we successfully purified a stable zGPR4–G<sub>s</sub> complex potentially due to the NanoBiT method designed to enhance GPCR–G protein stability.

Density maps were reconstructed to resolutions of 3.3 Å and 3.1 Å for pH 6.5 and pH 8.5, respectively (Fig. 1a, b and Supplementary Table 1). Although overall map quality for the pH 8.5 structure is slightly better than the map of the pH 6.5 structure in the transmembrane region, it is relatively poorer in the extracellular loops (ECLs), likely due to a relatively higher entropic nature of these loops at neutral pH (Fig. 1c, d and Supplementary Fig. 2). The two structures are almost identical in the receptor’s transmembrane region and the G protein (Fig. 1e, f). There is slight orientational difference between G protein subunits Gα and Gβ potentially attributed to the two buffers used perturbing the interactions between the G protein subunits (Fig. 1e), this should not be physiologically relevant as the G protein subunits may not experience similar pH change intracellularly. Also, the receptor–Gα<sub>s</sub> interface is quite identical under pHs of 6.5 and 8.5, suggesting the intracellular G protein-coupling is anyhow insensitive to pH change. As most of the ECL residues could be modeled in the pH 6.5 structure (named zGPR4<sup>6.5</sup> hereafter), we will mainly discuss this model unless otherwise specified.

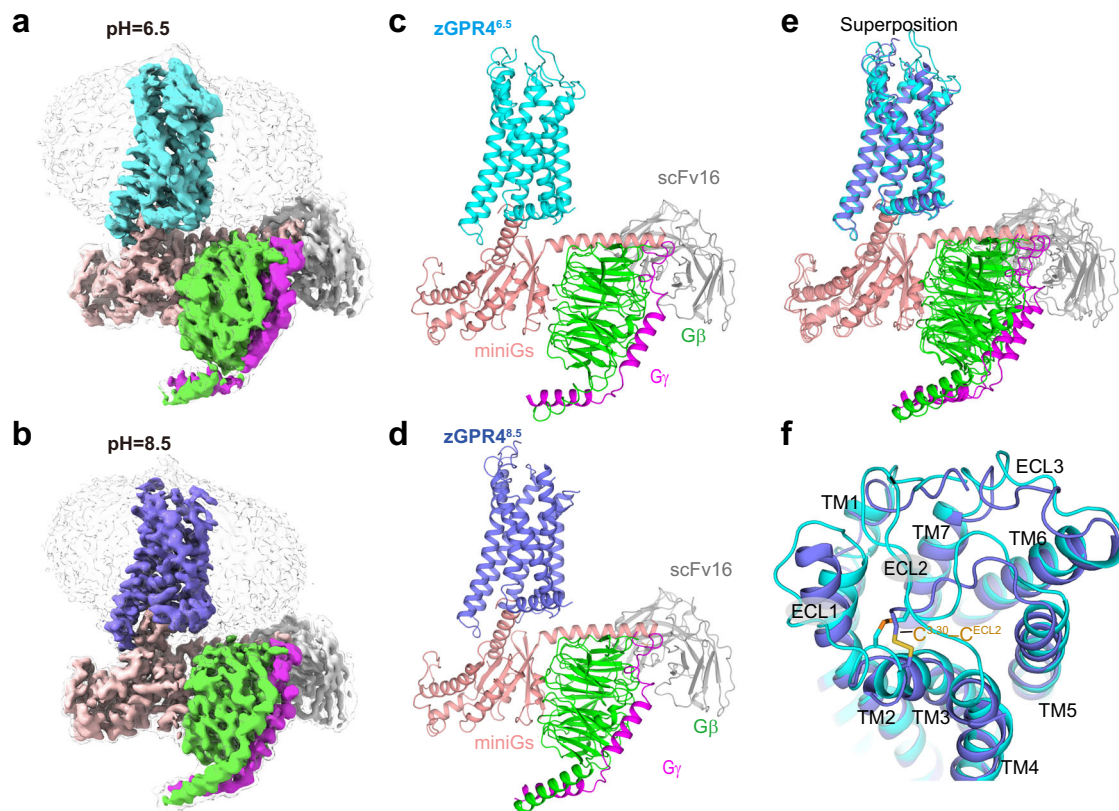


**Fig. 1 | Overall structures of G<sub>s</sub>-coupled zGPR4 under pH 6.5 and 8.5.** a–d Cryo-EM maps showing the disk-shaped micelle (left) and cartoon representation (right) of the zGPR4–G<sub>s</sub> complexes under pH 6.5 (a, c) and pH 8.5 (b, d). e, f Superposition

of the two structures at pH 6.5 and 8.5 on side view (e) or extracellular view (f). The disulfide bond is shown in stick.

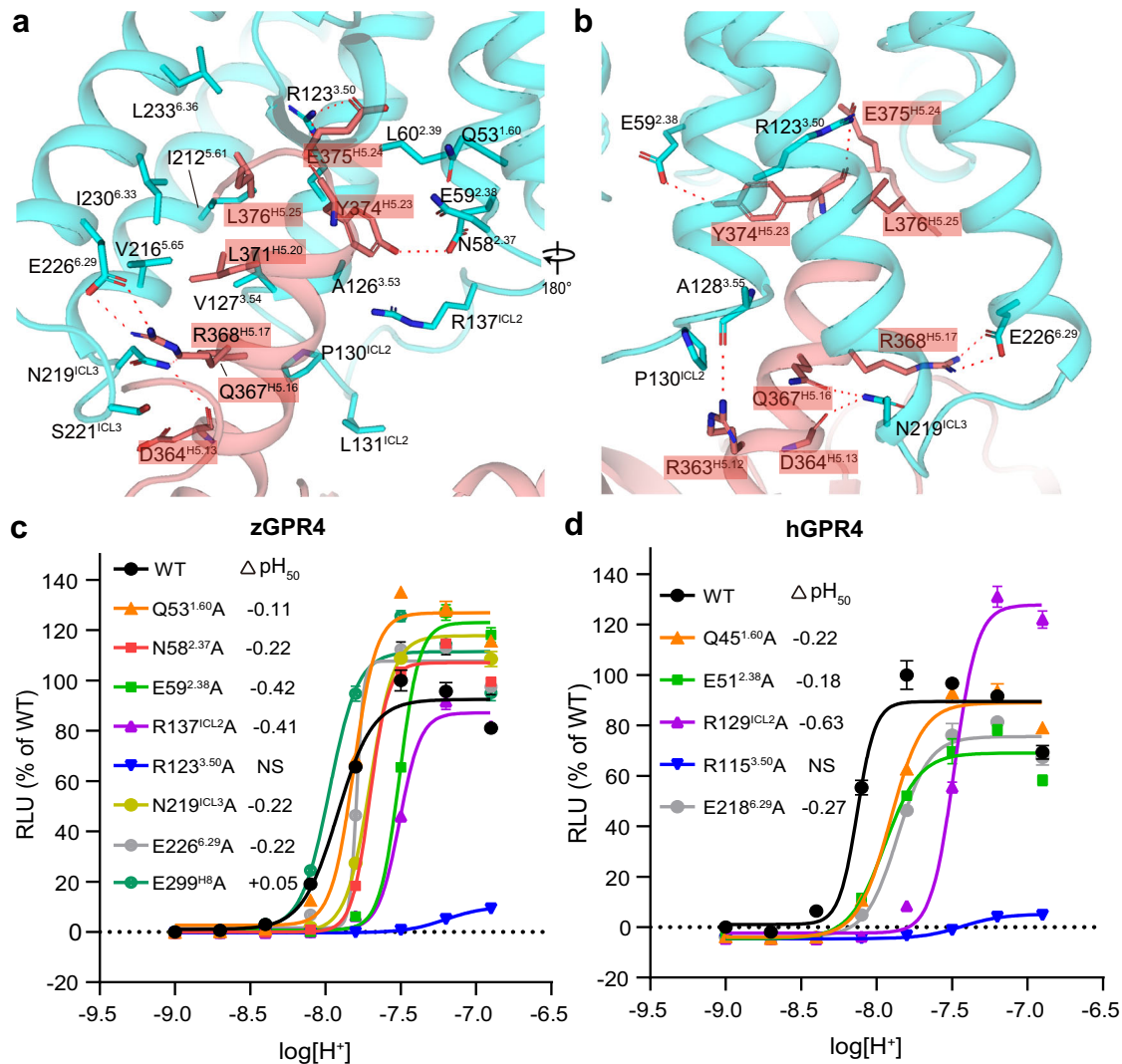


**Fig. 2 | The  $G_s$ -binding interface of zGPR4.** **a, b** The receptor- $\alpha_5$  interface in zGPR4<sup>6,5</sup>. Interacting residues are shown as sticks and are labeled. **c, d** Mutagenesis analysis of residues in zGPR4 (**c**) and hGPR4 (**d**) on the potency of G protein-coupling by the GloSensor cAMP assay. The maximum and minimum activation

levels of WT GPR4 were set to 100 and 0%, respectively. The  $\Delta pH_{50}$  was calculated by dividing the potency ( $pH_{50}$ ) of the mutant by the  $pH_{50}$  of WT. Data are shown as means  $\pm$  SEM from at least three independent experiments performed in triplicate. Source data are provided as a Source Data file.

### Receptor-G protein interface

At the receptor- $G\alpha_s$  interface, there are several polar residues on the receptor side interaction with the  $\alpha_5$  helix of  $G\alpha_s$  (Fig. 2a, b). For example, N219<sup>ICL3</sup> and E226<sup>6.29</sup> (Ballesteros-Weinstein numbering in superscript<sup>22</sup>) of zGPR4 form a hydrogen bond or salt bridge with D364<sup>H5.13</sup> and R368<sup>H5.17</sup> (superscript refers to common G protein numbering<sup>23</sup>) of  $\alpha_5$ , respectively. Notably, the highly conserved R123<sup>3.50</sup> of zGPR4 engages in both a salt bridge with E375<sup>H5.24</sup> and a  $\pi$ -cation interaction with the landmark residue of  $\alpha_5$ , Y374<sup>H5.23</sup>. The side chain of Y374<sup>H5.23</sup> shifts toward ICL1, establishing hydrogen bond connections with Q53<sup>1.60</sup>, N58<sup>2.37</sup>, and E59<sup>2.38</sup>. Additionally, there is a conserved hydrophobic interaction network between L371<sup>H5.20</sup> and L376<sup>H5.25</sup> of  $\alpha_5$  helix and zGPR4 residues V127<sup>3.54</sup>, I212<sup>5.61</sup>, V216<sup>5.65</sup>, I230<sup>6.33</sup>, and L233<sup>6.36</sup>. Mutagenesis data confirmed the importance of these residues. The previously characterized essential residue for G protein-coupling, R123<sup>3.50</sup>, if mutated, nearly abolished the capability of zGPR4 to couple to downstream  $G_s$  protein (Fig. 2c). Other tested mutants (Q53<sup>1.60</sup>A, N58<sup>2.37</sup>A, E59<sup>2.38</sup>A, R137<sup>ICL2</sup>A, N219<sup>ICL3</sup>A, E226<sup>6.29</sup>A) can shift the  $pH_{50}$  downward to different extents (0.2–0.5 log units) (Fig. 2c), suggesting these mutations compromise the receptor's sensitivity to proton

concentration by 1.6–3.2 folds. hGPR4 mutations yielded consistent results with those observed for zGPR4 (Fig. 2d), indicating that the chimera complex of zGPR4- $G_s$  indeed mirrors how hGPR4 interacts with its downstream G protein.

Our zGPR4- $G_s$  structures reveal a non-canonical  $G_s$ -coupling model for zGPR4, with the intercellular tip of TM5-TM6 gently moving outward to accommodate the  $G\alpha_s$  protein ( $\sim 4$  Å) compared to an inactive zGPR4 model from AlphaFold) (Fig. 3a, b). This differs from canonical GPCR- $G_s$  complexes, where TM6 undergoes more pronounced movements (12–16 Å) (Fig. 3c). However, the C-terminal tip of the  $\alpha_5$  helix in the zGPR4- $G_s$  complex assumes a similar hook structure to that observed in canonical  $G_s$ -coupled receptors, albeit moving 5–6 Å toward TMs 1 and 2 due to the smaller intracellular pocket in zGPR4 (Fig. 3c, embedded). In this regard, the zGPR4- $G_s$  structure bears closer resemblance to previously characterized GPCR- $G_i$  complexes (Supplementary Fig. 3a, b), including the recently determined GPR132- $G_i$  complex structure<sup>24</sup> (Supplementary Fig. 3c). Our structure, in conjunction with recently solved complex structures with non-canonical  $G_s$ -coupling model (e.g., GPR174, EP2, CCKAR), suggests that a larger

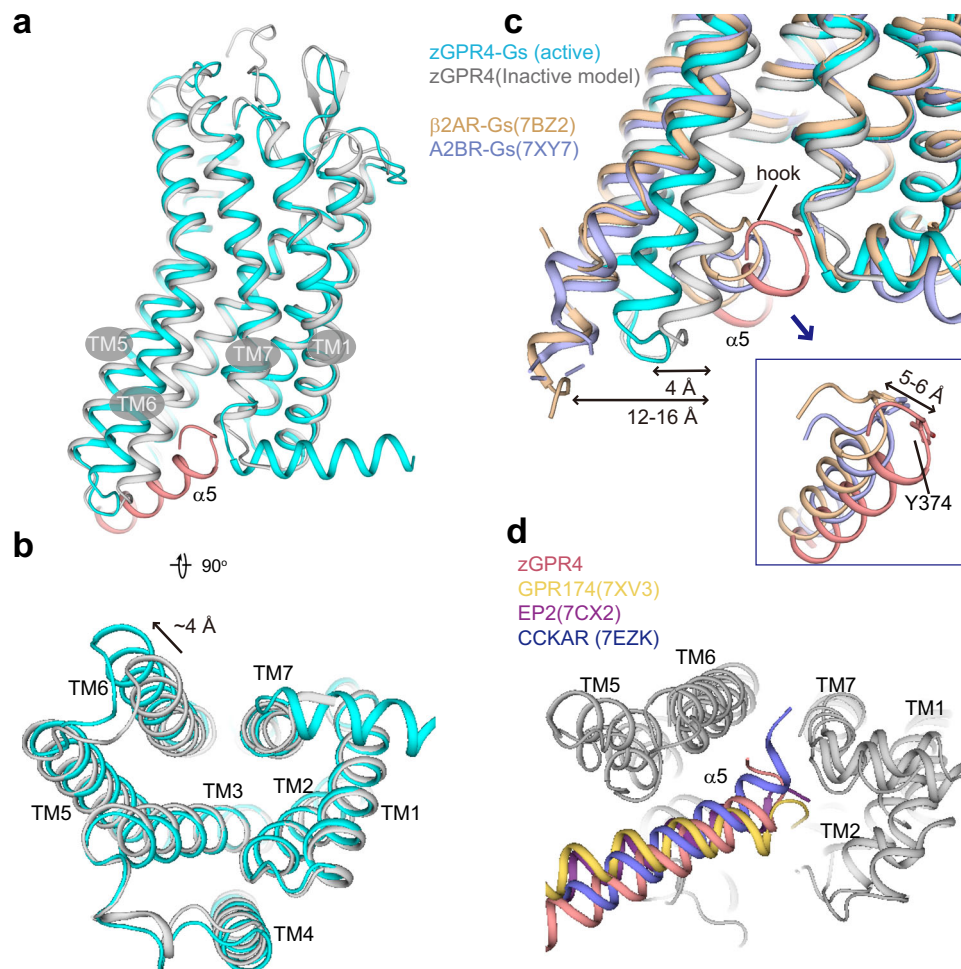


**Fig. 3 | Structural comparison for zGPR4.** **a, b** Superposition of the active zGPR4-G<sub>s</sub> structure with its inactive model (AlphaFold). **c** The two zGPR4 models are further compared with the  $\beta_2$ AR (PDB ID: 7BZ2) and A<sub>2</sub>BR (PDB ID: 7XY7) structures. **d** Alignment of zGPR4-G<sub>s</sub> (current study) with other non-canonical G<sub>s</sub>-

coupled structures, including GPR174 (PDB ID: 7XV3), EP2 (PDB ID: 7CX2) and CCKAR (PDB ID: 7EZK). Color codes are indicated at the top-left corner. For clarity, only  $\alpha 5$  helix is shown in each G<sub>s</sub>-coupled structure.

outward movement of the intercellular TM5-TM6 is not a prerequisite for G<sub>s</sub> protein recruitment (Fig. 3d)<sup>25</sup>.

### Structural features

In the zGPR4<sup>6,5</sup> structure, we were able to model the conserved disulfide bond between TM3 and ECL2 (C98<sup>3,25</sup>-C176<sup>45,50</sup>) (Fig. 1f). Although the last modeled residue at the N-terminus (C17) is proximal to C266 of ECL3, weak density precluded confirmation of a disulfide bond between them. Nevertheless, sequence alignment and structural prediction indicated a conserved disulfide linkage between the two positions for psGPCRs (Supplementary Fig. 4). Through cAMP assays, we found either C17S or C266S on zGPR4 had no significant impact on proton potency or efficacy (Supplementary Figs. 5 and 6), in contrast to the reduced activities for the corresponding mutations on GPR68<sup>16</sup>. zGPR4 features two additional cysteines (C11, C264) neighboring the aforementioned cysteines compared to hGPR4 (Supplementary Fig. 4), potentially adding complexity to the aspect of disulfide linkage in zGPR4. Alternatively, with two potential disulfide linkages between ECL3 and the N-terminus in zGPR4, breakage of a single disulfide bond may not be essential to destroying the structural rearrangement for receptor activation.

The zGPR4<sup>6,5</sup> structure features a partially ordered ECL2 that covers the orthostatic pocket. A cluster of bulky residues within ECL2, including F175, F177, E178, K179 and Y180, obstructs the pathway to the

canonical orthostatic pocket (Fig. 4a). The F175 and Y180 form an aromatic triangle with a TM7 residue F273<sup>7,32</sup>. Remarkably, the F177<sup>45,51</sup> that inserted into the pocket is highly conserved among the proton-sensing receptors, indicating an indispensable role for this residue for the structural integrity of these receptors. Both the zGPR4<sup>6,5</sup> active structure and its inactive model reveal a predominantly covered orthostatic pocket that rich in bulky aromatic residues (Fig. 4a), reminiscent of lipid-binding GPCRs and olfactory receptors. The orthosteric pocket volume of zGPR4 is only 166 Å<sup>3</sup>, relatively smaller than the size of adenosine A<sub>2A</sub> receptor (A<sub>2A</sub>R, 272 Å<sup>3</sup>)<sup>26</sup> and  $\beta_2$  adrenergic receptor ( $\beta_2$ AR, 313 Å<sup>3</sup>)<sup>27</sup>, and much smaller than these peptidic GPCRs (neurokinin 1 receptor, 651 Å<sup>3</sup>; angiotensin II receptor type 1, 1346 Å<sup>3</sup>)<sup>28,29</sup> (Supplementary Fig. 7). Since GPR4 senses one of the smallest stimuli (proton) for its activation, such a compact structure within the pocket may facilitate a Van der Waals interaction network between TMs, transmitting the signal of protonation from the extracellular to the intercellular for conformational change. Although in both maps the electron density for the extracellular half is relatively poor compared to the intercellular half, the key motifs within the signaling transduction pathway are relatively clear, including the toggle switch, the PIF motif, and the DPxxY motif. The F<sup>5,50</sup>[<sup>3,40</sup>F<sup>6,44</sup> motif is unique in GPR4 within proton-sensing receptors (Supplementary Fig. 8). In GPR4, the position of F<sup>6,44</sup> is replaced by a short residue, V241<sup>6,44</sup>; in contrast, the encountering residue of V241<sup>6,44</sup> in TM5 is a

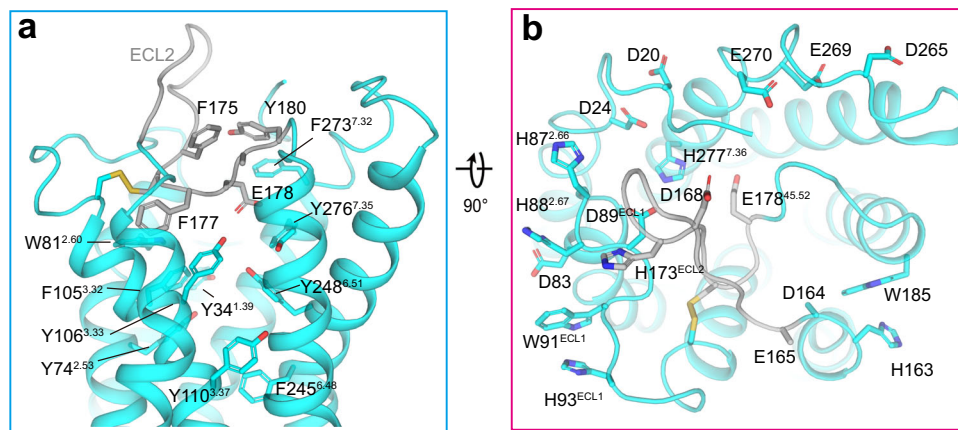


**Fig. 4 | Structural features for zGPR4. a** Side view of the zGPR4 orthostatic pocket showing a bunch of aromatic residues. **b** Extracellular view of the zGPR4 showing the titratable H/D/E residues at the ECLs. Some key interacting residues are also shown. **a, b** The ECL2 is colored gray for clarity.

bulky residue (W202<sup>5.51</sup>) that is usually occupied by a hydrophobic aliphatic residue (like V/L) in other class A GPCRs. W<sup>5.51</sup> and V<sup>6.44</sup> are highly conserved across different species of GPR4, confirming the significance of these positions for the signal propagation pathway, and evolving in tandem to adapt to environmental changes.

Extracellular regions were suggested to sense the protons thus triggering the conformational change for activation. Previous work have identified the protonation of H79<sup>2.66</sup>, H165<sup>ECL2</sup>, and H269<sup>7.36</sup> residues of hGPR4 as critical for its activation<sup>18</sup>. Similarly, the residue corresponding to H79 in zGPR4 (H87<sup>2.66</sup>) has also proved to be essential<sup>30</sup>. Nevertheless, we found in our active structure of zGPR4<sup>6.5</sup> the histidine residues are far apart: H173<sup>ECL2</sup> of ECL2 is 5–6 Å away from H87<sup>2.66</sup> or H88<sup>2.67</sup>, and even farther from H93<sup>ECL1</sup>, H277<sup>7.36</sup> and H163<sup>4.63</sup> (Fig. 4b). Among them, H93<sup>ECL1</sup> and H163<sup>4.63</sup> appear to play essential structural roles together with the aromatic residues W91<sup>23.50</sup> and W185<sup>5.34</sup>. Also, there are many acidic residues in the extracellular region, and D24<sup>1.31</sup>, D89<sup>ECL1</sup>, D168<sup>ECL2</sup>, and E178<sup>45.52</sup> are located around the previously suggested histidine cluster (Fig. 4b).

### Mutagenesis studies of featured residues

Our mutagenesis data demonstrate reduced proton potency by 0.2–0.3 log units for zGPR4 mutations H87<sup>2.66</sup>F and H173<sup>ECL2</sup>F, and negligible effect for H277<sup>7.36</sup>F (Fig. 5a), consistent with previous results<sup>18</sup>. Among these acidic residues at the extracellular region, Mutations at E178<sup>45.52</sup> (E178<sup>45.52</sup>Q, E178<sup>45.52</sup>A) can each decrease proton potency by 0.2–0.3 log unit while maintaining the maximal efficacy (Emax), suggesting that E178<sup>45.52</sup> facilitates the sensing of protons (Fig. 5b). Located centrally in ECL2, E178<sup>45.52</sup> is surrounded by several polar residues including K179<sup>45.53</sup>, Y106<sup>3.33</sup>, R255<sup>6.59</sup> and H277<sup>7.36</sup>, indicating this acidic residue likely contributes to charge-charge interactions that was not fulfilled by a glutamine or an alanine. Interestingly, we found both D89<sup>ECL1</sup>N and D89<sup>ECL1</sup>A mutations significantly increase proton sensitivity (0.4–0.5 log unit), implying that this acidic residue somehow disturbs proton-sensing (Fig. 5b). Similar as D89<sup>ECL1</sup>, we found a double mutant D164<sup>ECL2</sup>N&E165<sup>ECL2</sup>Q can also increase proton sensitivity (0.25 log unit) (Fig. 5c). These four acidic residues at the extracellular region are absolutely conserved among psGPCRs (Supplementary Fig. 4). Mutations of additional three acidic residues, D24<sup>NT</sup>N, D169<sup>ECL2</sup>N, E183<sup>ECL2</sup>Q, do not induce significant change on proton potency, whereas the former two can increase the efficacy compared to WT receptor (Fig. 5c). These results indicate that most extracellular acidic residues do not contribute essentially for proton-sensing.

An acidic triad (E<sup>4.53</sup>, D<sup>2.50</sup>, D<sup>7.49</sup>) within the core of 7TM is important for the proton-induced activation, and mutations of these residues to glutamine or asparagine (to mimic their neutral form) induce upward

shift in EC<sub>50</sub><sup>19</sup>. The latter two are shown to be directly coordinated with a Na<sup>+</sup> (together with S<sup>3.39</sup>) in the inactive state of typical GPCRs, whereas in the active state the sodium was extruded as a result of conformational change<sup>31</sup>. Interestingly, in GPR4 as well as other proton-sensing GPCRs, the canonical N<sup>7.49</sup>PxxY<sup>7.53</sup> motif is replaced by a D<sup>7.49</sup>PxxY<sup>7.53</sup> motif (Supplementary Fig. 4). To investigate the function of D290<sup>7.49</sup> we conducted two mutations, D290N and D290A. The results of cAMP assays showed that while both mutants were expressed at similar levels as the WT receptor (Supplementary Fig. 6), the D290<sup>7.49</sup>N shifted the pH<sub>50</sub> upward from 7.7 to 8.1 (Fig. 5d), consistent with the corresponding mutations reported previously<sup>19</sup>. Meanwhile, the basal activity of D290<sup>7.49</sup>N is also significantly elevated compared to WT. In contrast, the D290<sup>7.49</sup>A mutant compromised both the proton potency and Emax. These results indicate that the D<sup>7.49</sup>N mutation may loosen the restraint by sodium, making the receptor more easily activated; on the contrary, the D<sup>7.49</sup>A mutation may disturb the local structure as well as the conformational transition from inactive to active. Furthermore, mutations of the key sodium coordination site by D71<sup>2.50</sup>A or D71<sup>2.50</sup>N can each significantly decrease the proton potency and Emax (Fig. 5d), this can be attributed to the similar reason as the D<sup>7.49</sup>A mutant. Similarly, a subsidiary sodium coordination residue, N286<sup>7.45</sup>, can shift the pH<sub>50</sub> downward when substituted by alanine (Fig. 5d), indicating it may function by affecting the pK<sub>a</sub> (where Ka is the acid dissociation constant) of its nearby sodium coordination residue, e.g., the D290<sup>7.49</sup>.

Unexpectedly, we found that mutations of the bulky aromatic residues within the orthosteric pocket can consistently increase the proton potency of zGPR4 (Fig. 5e). While the increments by Y110<sup>3.37</sup>F and Y276<sup>7.35</sup>F are not significant (< 0.1 log units), Y106<sup>3.33</sup>F and Y248<sup>6.51</sup>F can each increase the pH<sub>50</sub> by ~0.3 log unit. Y106<sup>3.33</sup> and Y248<sup>6.51</sup> face each other in the 7TM central region and Y110<sup>3.37</sup> and Y276<sup>7.35</sup> are located below and above them (Supplementary Fig. 8). Since Y248<sup>6.51</sup> is one helical turn above the toggle switch residue F245<sup>6.48</sup>, these aromatic residues may contribute to a Van der Waals interaction network within the pocket that propagates the signal of proton-sensing to the intercellular region. These results further indicate that the propagation in the central region may not rely on the hydrophilic properties of these residues; alternatively, these tyrosines may already contribute to a hydrophilic interaction network in the inactive state and their mutations to phenylalanine facilitate the transition to active state (Supplementary Fig. 8).

### Implications for activation pathway

There are many histidines and acidic residues at the extracellular region, which possess different charge states at different pH: histidine is neutral at high pH but positively charged when protonated at pH < 7.0, whereas extracellular acidic residues consistently maintain a

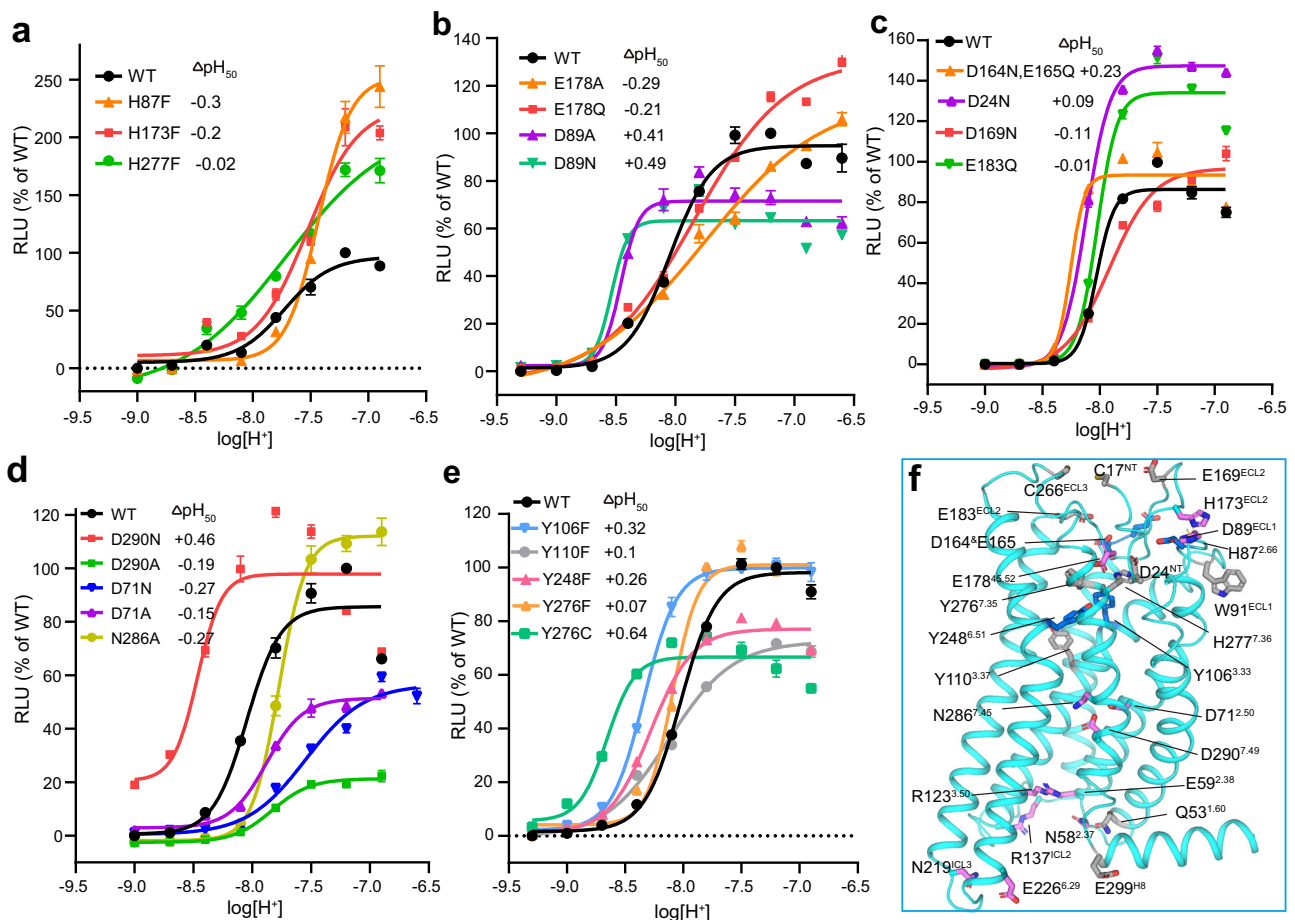


**Fig. 5 | Mutagenesis analysis of featured residues on zGPR4.** **a–e** Mutagenesis analysis of residues in zGPR4 on the proton potency by the GloSensor cAMP assay. Mutagenesis analysis of histidine residues in ECLs (**a**), highly conserved acidic residues in ECLs (**b**), partially conserved acidic residues (**c**), the Na coordinating residues (**d**), and the aromatic residues within the orthosteric pocket (**e**). The maximum and minimum activation levels of WT GPR4 were set to 100 and 0%, respectively. The  $\Delta\text{pH}_{50}$  was calculated by dividing the  $\text{pH}_{50}$  of the mutant by the

$\text{pH}_{50}$  of WT. Data are shown as means  $\pm$  SEM from at least three independent experiments performed in triplicate. **f** Mapping the tested mutations on the zGPR4 structure. Mutations with positive effect ( $\Delta\text{pH}_{50} > 0.2$  unit) are colored blue; mutations with negative effect ( $\Delta\text{pH}_{50} < -0.2$  unit) are colored red; mutations with negligible effect ( $0.2 > \Delta\text{pH}_{50} > -0.2$ ) are colored gray. Source data are provided as a Source Data file.

negative charge within the physiological pH range. Nevertheless, our results indicate that WT GPR4 has a  $\text{pH}_{50}$  of -8, contrasting with lower  $\text{pH}_{50}$  values of 7–7.4 for GPR65 and 6.3–6.7 for GPR68<sup>19,32</sup>. This suggests that GPR4 activation might not rely on protonation of extracellular histidines, given its  $\text{pK}_a$  of around 7. Moreover, studies showed that extracellular histidines in psGPCRs are largely unconserved, and even conserved histidines produce varied pharmacological effects upon mutation<sup>19</sup>. These findings imply that extracellular histidines are unlikely to be key proton sensors. Notably, we found mutations of extracellular histidines as well as acidic residues moderately influenced zGPR4's potency or efficacy (Fig. 5f), but we did not identify any single mutation that completely abolish the function of zGPR4—unlike the almost abrogation by R123<sup>3.50</sup>A in the G protein-coupling region. This suggests that these H/D/E residues may primarily fine-tune the receptor's transition from inactive to active conformations rather than mediate proton-sensing.

In contrast, mutations at the so-called “DyaD” site (D71<sup>2.50</sup>, D290<sup>7.49</sup>) influenced receptor function more significantly. Specifically, mutations at D71<sup>2.50</sup> severely compromised efficacy, while the D290<sup>7.49</sup>A and D290<sup>7.49</sup>N mutations produced opposing effects on receptor's proton-sensing ability. These data are in favor of the conclusion that proton-sensing is primarily mediated by the acidic triad residues within the transmembrane domain<sup>19</sup>. Notably, we found the Y-

to-F mutations within the orthosteric pocket enhanced the potencies. This indicated that, instead of a water-mediated hydrophilic network, the central region of psGPCRs mainly used bulky sidechains to propagate the signaling transduction (Supplementary Fig. 8). Remarkably, we found a mimicking mutation (Y276<sup>7.35</sup>C) of a natural genetic variation of hGPR4 can further increase the  $\text{pH}_{50}$  compared to Y276<sup>7.35</sup>F (Fig. 5e), while the mutation has negligible effect on expression or  $E_{\text{max}}$  (Supplementary Fig. 6), suggesting the mutant may function simply by favoring the active state. Other natural genetic variations are mostly located in the central region of the 7TM (Supplementary Fig. 9), and we can expect that some of them may facilitate the transition from inactive to active, while some may hamper the transition.

## Discussion

Here we report cryo-EM structure of active zGPR4 in complex with an engineered  $G_s$  protein. Compared to the inactive AlphaFold model of zGPR4, the ECLs experience relatively larger conformational changes than the transmembrane region. Generally, GPCR activation involves contraction of the 7TM central region and expansion of the extracellular and intracellular regions, which is required to provide space for accommodating the G protein. Sodium acts as a negative allosteric modulator for many class A GPCRs, coordinating with key positions

(including 2.50, 3.39, and 7.49) in the inactive state, and is displaced during the transition to the active state<sup>31</sup>. Buried within the 7TM central region, the  $pK_a$  of the acidic triad residues likely shifts to the physiological pH range<sup>33</sup>, meaning that protonation at lower pH neutralizes their charge, and preventing D<sup>2.50</sup> and D<sup>7.49</sup> from coordinating with positively charged sodium (or potassium) ions. Consequently, a reduction in pH can disrupt sodium coordination essential for receptor activation. Given the conserved nature of the DyaD site (D<sup>2.50</sup> is highly conserved among class A GPCRs, D<sup>7.49</sup> is half-conserved in  $\delta$ -branch receptors), the unique apEx site (E<sup>4.53</sup>) of the acidic triad within psGPCRs likely plays a significant role in signaling transduction, as only these three receptors are fully activated by protons. The molecular details may still await further investigation.

We observed distinct effects from D-to-N mutations at the DyaD sites: D<sup>7.49</sup>N increased the potency, contrasting with reduced potency from D<sup>2.50</sup>N mutation. Previous structural studies have shown that an acidic residue at position 7.49 participates in a direct coordination with the sodium in receptors like cysLT1<sup>34</sup>, PAR1<sup>35</sup>, and PAR2<sup>36</sup>, forming an additional coordination bond compared to receptors with a neutral residue (N<sup>7.49</sup>)<sup>37–39</sup>. Therefore, D<sup>7.49</sup>N is suggested to loosen the coordination with the sodium, making the receptor more readily activated. The tight coordination by D<sup>7.49</sup> is thought to stabilize the inactive conformation, this could be the reason that many  $\delta$ -branch receptors exhibit low basal activity<sup>40</sup>. In contrast, D<sup>2.50</sup>N as well as D<sup>2.50</sup>A may have totally disrupted the coordination, as evidenced by diminished sodium regulation in mutagenesis studies of psGPCRs and other GPCRs<sup>19,31</sup>. The reduction in efficacy for zGPR4 due to D<sup>2.50</sup>N or D<sup>2.50</sup>A mutations is consistent with compromised G protein signaling observed in other receptors<sup>31</sup>. The essential role of D<sup>2.50</sup> is also underscored by its high conservation across class A GPCRs, whereas D<sup>7.49</sup> is only half-conserved in  $\delta$ -branch receptors (including psGPCRs), with other subfamilies predominantly featuring N<sup>7.49</sup>.

Beside protons, lysolipids were also suggested as “ligands” for psGPCRs. Our structures of zGPR4 reveal a tiny orthosteric pocket composed of highly conserved aromatic residues within the psGPCR family (Supplementary Fig. 7), which provided a hydrophobic platform to accommodate their potential lipidic ligands. Also, several other receptors (e.g., GPR31 and GPR151) were found to be activated under acidic conditions *in vitro*, although the GPR31 has been reported as a receptor for endogenous lipid, 12-(S)-hydroxyeicosatetraenoic acid<sup>41,42</sup>. These findings indicate that proton-sensing may be one of many properties of GPCRs and that other proton-sensing GPCRs may exist that allow detection of a broader pH range.

GPR4 has been linked to several pH-dependent processes under pathological conditions, including modulation of inflammation, angiogenesis and tumor metastasis. In addition, GPR4 has also been identified as a biomarker for neurodegenerative diseases like Parkinson's and Alzheimer<sup>43</sup>, and inhibition of GPR4 was shown to reduce neuronal apoptosis and improve memory functions<sup>44</sup>. These studies underscored the potential therapeutic relevance of antagonists or negative allosteric modulators aimed at inhibiting GPR4 activity or expression across various tissues. Nevertheless, our findings reveal that both hGPR4 and zGPR4 have a  $pH_{50}$  of ~8.0, meaning they are constitutively active at a physiological pH of 7.4. This implies that proton-sensing may not be directly related to their biological function, unlike other psGPCRs such as GPR65 and GPR68, which are activated by changes in physiological pH. That is to say, these psGPCRs may be activated to different levels and thus function differently at various pH conditions. In addition, GPR4 may play some unique roles within the physiological environment in response to other ligands like lysolipids.

In summary, our data support the conclusion that these psGPCRs share a common triad acidic residue essential for proton-sensing<sup>19</sup>, while the varying amount of histidines and nearby acidic residues likely act as modulators of receptor function. A cluster of aromatic residues within the orthosteric pocket also contributes to the propagation of

signaling across the transmembrane domain. The GPR4 structures together with assay results provided a framework for further understanding of the proton-sensing mechanism as well as development of small molecular modulators for these psGPCRs.

### Limitations of current study

Our study has some limitations. Firstly, the resolution is insufficient to determine the protonation status of protonatable residues, preventing us from confidently identifying which residues are key for proton-sensing. Second, to obtain the structure, we had to expose both sides of the GPCR to the same pH change, which does not occur under physiological conditions, this limitation constrains our structural interpretations. Lastly, our structure only captures the active state of the receptor. Since proton-sensing relies on (de)protonatable residues with  $pK_a$  values that differ significantly between inactive and active states, this further complicates our ability to identify specific residues responsible for proton-sensing from our structural data. Nevertheless, our structures may still serve as a valuable resource for comparative analyses of other proton-sensing GPCRs from different species.

## Methods

### Construct cloning, expression, and purification of zGPR4-G<sub>s</sub> complexes

For the receptor, zebrafish GPR4 (residues 2–338), containing an N-terminal thermostabilized apocytochrome b<sub>562</sub>RIL fusion protein and a C-terminal LgBiT protein, was cloned into pFastBac1 vector, with an N-terminal hemagglutinin signal peptide tag followed by FLAG tag and C-terminal 10 × His tag. For the G protein components, mini-G<sub>s</sub>IN, equal to mini-G<sub>s</sub> but with its  $\alpha$ N replaced by the counterpart of G<sub>i</sub> (to facilitate binding of scFv16, which binds to the interface between G $\beta$ y subunits and G $\alpha_i$  subunit)<sup>45</sup>, was fused to bovine G $\gamma$ 2 at its N-terminus (G $\gamma$ -mini-G<sub>s</sub>IN). Human G $\beta$ 1, followed by SmbiIT at its C terminus, was cloned into pFastBac-Dual together with G $\gamma$ -mini-G<sub>s</sub>IN. Sf9 insect cells were infected with viruses of the receptor (zGPR4-LgBiT) and G $\gamma$ -mini-G<sub>s</sub>IN-G $\beta$ -SmbiIT in the ratio of 1:1 for 72 h at 27 °C.

For the zGPR4<sup>6.5</sup> complex, the cell pellets were lysed by Dounce homogenization in 20 mM MES (pH 6.5), 100 mM NaCl, 5 mM MgCl<sub>2</sub>, 5 mM CaCl<sub>2</sub>, 10% glycerol, EDTA-free protease inhibitor cocktail (Bimake), apyrase (25 mU/ml; New England Biolabs), 200  $\mu$ M Tris(2-carboxyethyl)phosphine (TCEP) (Thermo Fisher Scientific), and scFv16 (15  $\mu$ g/ml), incubated at 4 °C for 3 h, and then centrifuged at 30,000 rpm for 45 min to collect the membranes. The washed membranes were solubilized in 20 mM MES (pH 6.5), 100 mM NaCl, 5 mM MgCl<sub>2</sub>, 5 mM CaCl<sub>2</sub>, EDTA-free protease inhibitor cocktail, 1% (w/v) lauryl maltose neopentyl glycol (LMNG; Anatrace), 0.2% (w/v) cholesteryl hemisuccinate (CHS; Sigma-Aldrich), apyrase (25 mU/mL), and 200  $\mu$ M TCEP and incubated at 4 °C for 3 h. The supernatant was collected by centrifugation at 30,000 rpm for 45 min and then incubated with TALON immobilized metal affinity chromatography resin (Clontech) with an addition of 20 mM imidazole at 4 °C overnight. The resin was collected by centrifugation at 1000 × g for 5 min, packed into a gravity flow column, and washed with 20 column volumes of buffer containing 20 mM MES (pH 6.5), 100 mM NaCl, 2 mM MgCl<sub>2</sub>, 2 mM CaCl<sub>2</sub>, 0.01% (w/v) LMNG, 0.002% (w/v) CHS, 5% glycerol, and 30 mM imidazole and eluted using buffer containing 20 mM MES (pH 6.5), 100 mM NaCl, 2 mM MgCl<sub>2</sub>, 2 mM CaCl<sub>2</sub>, 0.01% (w/v) LMNG, 0.002% (w/v) CHS, 5% glycerol, and 300 mM imidazole. The purified zGPR4-G<sub>s</sub> complex and scFv16 proteins were mixed in a 1:1 molar ratio at 4 °C overnight and then concentrated with an Amicon Ultra Centrifugal Filter [molecular weight cutoff (MWCO), 100 kDa] and subjected to size-exclusion chromatography (SEC) using a Superdex 6 10/300 GL column (GE Healthcare) with running buffer, containing 20 mM MES (pH 6.5), 100 mM NaCl, 2 mM MgCl<sub>2</sub>, 0.0025% (w/v) LMNG, and 0.0005% (w/v) CHS. The fractions of monomeric protein complex

were pooled and concentrated with an Amicon Ultra Centrifugal Filter (MWCO, 100 kDa) to 12 to 16 mg/ml for cryo-EM studies.

For the zGPR4<sup>8.5</sup> complex, the purification process was similar to that of zGPR4<sup>6.5</sup>, except that MES (pH 6.5) was replaced by Tris (pH 8.5). Finally, the fractions of monomeric protein complex were pooled and concentrated with an Amicon Ultra Centrifugal Filter (MWCO, 100 kDa) to 6 to 9 mg/ml for cryo-EM studies.

### Cryo-EM grid preparation and data collection

For sample preparation, 3  $\mu$ l of purified zGPR4<sup>6.5</sup> and zGPR4<sup>8.5</sup> were applied onto the glow-discharged holey grids (Ni-Ti Au 300 mesh, NANODIM TECH), respectively. The grids were blotted for 3 s under 100% humidity at 4 °C and then plunge-frozen into liquid ethane using Vitrobot Mark IV (Thermo Fischer Scientific). The cryo-EM data were collected at the Center of Cryo-Electron Microscopy at Zhejiang University. Micrographs were acquired on the Titan Krios microscope (FEI) operated at 300 kV equipped with Selectris energy filter (Thermo Fisher Scientific) and Gatan Falcon 4 detector. EPU software was used for automated data collection according to standard procedures. A calibrated magnification of  $\times 130,000$  was used for imaging, yielding a pixel size of 0.931 Å on images. Each micrograph was dose-fractionated to 40 frames at a dose rate of 7.49 e<sup>-</sup> per pixel per second, with a total exposure time of 6 s, resulting in a total dose of about 52 e<sup>-</sup> Å<sup>-2</sup>. The defocus range was set from -1.0 to -2.0  $\mu$ m.

### Cryo-EM image processing

Image processing was conducted using cryoSPARC v4.4.1<sup>46</sup>. Motion correction and contrast transfer function (CTF) parameters estimation were performed with the MotionCorr2<sup>47</sup> and patch CTF estimation<sup>48</sup>, respectively.

For zGPR4<sup>6.5</sup>, a total of 8143 micrographs were collected, and 11,069,919 particles were auto-picked and extracted. After several rounds of two-dimensional (2D) classification, 368,456 particles were further subjected to ab initio reconstruction to generate the initial maps. Subsequently, 183,055 particles were selected for non-uniform refinement under C1 symmetry, resulting in a density map with an overall resolution of 3.3 Å, estimated by the gold-standard Fourier shell correlation coefficient (FSC) of 0.143.

Similar procedures were applied to zGPR4<sup>8.5</sup>, a total of 5188 micrographs were collected and 7,819,042 particles were auto-picked and extracted. Following multiple rounds of 2D classification, 558,130 particles were selected for ab initio reconstruction. One subset, comprising 246,730 particles, was then subjected to non-uniform refinement, generating a map with a resolution of 3.1 Å.

### Model building and refinement

Structures predicted by AlphaFold<sup>49,50</sup> and A<sub>2B</sub>R-mini-G<sub>s</sub> (PDB code 7XY6)<sup>51</sup> were used as the starting models for model building and refinement against the electron density map of zGPR4<sup>6.5</sup>-G<sub>s</sub> and zGPR4<sup>8.5</sup>-G<sub>s</sub>. Models were docked into the EM density maps using Chimera<sup>52</sup>. Subsequently, iterative manual adjustments and rebuilding were performed in COOT<sup>53</sup> and phenix.real\_space\_refine in Phenix<sup>54</sup>. The final refinement statistics are provided in Supplementary Table 1. The structure figures were prepared by Chimera and PyMOL (<http://www.pymol.org>).

### Comparison of orthosteric pockets

Structures of four prototype class A GPCRs were taken to compare with GPR4: two small molecule receptors,  $\beta_2$ AR (PDB ID: 4LDO) and A<sub>2A</sub>R (PDB ID: 5G53); and two peptidic receptors, NK1R (PDB ID: 7P00) and AGTR1 (PDB ID: 7F6G). All selected structures are in a fully active state (have cytoplasmic protein partners) and are bound to endogenous ligands (or close analog of endogenous ligand, as in A<sub>2A</sub>R). Volumes of pockets were measured using the Schrödinger software

(Schrödinger Release 2023-4: Schrödinger, LLC, New York, NY, 2023). Structures were processed using the Protein Preparation Wizard tool<sup>55</sup>. The volumes were calculated using the SiteMap program<sup>56,57</sup>.

### GloSensor cAMP assay

In brief, HEK293 (obtained from certified cell bank at the Chinese Academy of Science and confirmed as negative for mycoplasma contamination) cells in a 6.0 cm dish were cotransfected with 1  $\mu$ g of zebrafish/human wild-type or mutated GPR4 plasmid and 1  $\mu$ g of the pGloSensor-22F cAMP plasmid (Promega, USA) using polyethylene (6  $\mu$ L, Yeasen, China). After incubating overnight, transfected cells were resuspended in DMEM added with 1% dialyzed FBS and then seeded into poly-l-lysine-coated 384-well plates (2  $\times$  10<sup>4</sup> cells/well) (Costar, USA) for 9–24 h. After removing the culture medium, the cells were incubated with GloSensor™ cAMP reagent (Promega, USA) made in assay buffer (pH 8.4) for 1.5 h at 37 °C. To ensure that assay buffers (30  $\mu$ L/well) were administered at the correct pH levels, GloSensor™ cAMP reagent was withdrawn from cell plates before adding assay buffer at predefined pH levels. Assay buffers were made using 1x HBSS mixed with different buffer agents for different pH levels, 10 mM HEPES and 10 mM MES for pHs 6.9–8.1, and 20 mM TAPS for pHs 8.2–9.3. Cytation 5 imaging reader (BioTek, USA) was utilized to continually monitor bioluminescence signals for 20–40 min.

### Cell surface expression measurement

Cell surface expression of zebrafish/human wild-type or mutated GPR4 was detected by flow cytometry. Briefly, HEK293 cells in a six-well plate were transfected with zebrafish/human wild-type or mutated GPR4 plasmid and cultured for 24 h. The transfected HEK293 cells were harvested by Cell Scraper (Costar, USA) and then washed twice with PBS buffer containing 1% (w/v) BSA. The cells were resuspended by 100  $\mu$ L PBS buffer containing 1% (w/v) BSA and then followed by the incubation with diluted (0.5  $\mu$ g per million cells in 100  $\mu$ L volume) PerCP/Cyanine5.5 anti-FLAG Tag antibody (BioLegend, USA) at 4 °C for 30 min. After washing as described above, fluorescently tagged cells (2  $\times$  10<sup>4</sup> cells per sample) were detected using an LSR Fortessa flow cytometer (BD Biosciences), and data were analyzed by FlowJo software (TreeStar Inc., Ashland, OR, USA). Quantification was performed using mean fluorescence intensity (MFI) values.

### Reporting summary

Further information on research design is available in the Nature Portfolio Reporting Summary linked to this article.

### Data availability

Atomic coordinates and structure factors for the complexes have been deposited in the Protein Data Bank with identification code **8ZFZ** (model of G<sub>s</sub>-coupled zebrafish GPR4 at pH 6.5) and **9J31** (model of G<sub>s</sub>-coupled zebrafish GPR4 at pH 8.5), and the corresponding electron microscopy maps have been deposited in the Electron Microscopy Data Bank under accession codes **EMD-60072** (cryo-EM structure of G<sub>s</sub>-coupled zebrafish GPR4 at pH 6.5) and **EMD-61104** (cryo-EM structure of G<sub>s</sub>-coupled zebrafish GPR4 at pH 8.5). All other data are available in the manuscript or supplementary materials. Source data are provided with this paper.

### References

1. Katritch, V., Cherezov, V. & Stevens, R.C. Structure-function of the G protein-coupled receptor superfamily. *Annu. Rev. Pharm. Toxicol.* **53**, 531–556 (2013).
2. Wacker, D., Stevens, R. C. & Roth, B. L. How ligands illuminate GPCR molecular pharmacology. *Cell* **170**, 414–427 (2017).
3. Venkatakrisnan, A. J. et al. Molecular signatures of G-protein-coupled receptors. *Nature* **494**, 185–194 (2013).

4. Sriram, K. & Insel, P. A. G protein-coupled receptors as targets for approved drugs: how many targets and how many drugs? *Mol. Pharm.* **93**, 251–258 (2018).
5. Im, D. S. Two ligands for a GPCR, proton vs lysolipid. *Acta Pharm. Sin.* **26**, 1435–1441 (2005).
6. Wei, W. C. et al. Coincidence detection of membrane stretch and extracellular pH by the proton-sensing receptor OGR1 (GPR68). *Curr. Biol.* **28**, 3815–3823.e3814 (2018).
7. Imenez Silva, P. H. & Wagner, C. A. Physiological relevance of proton-activated GPCRs. *Pflug. Arch.* **474**, 487–504 (2022).
8. Eltzschig, H. K. & Carmeliet, P. Hypoxia and inflammation. *New Engl. J. Med.* **364**, 656–665 (2011).
9. Boedtker, E. & Pedersen, S. F. The acidic tumor microenvironment as a driver of cancer. *Annu. Rev. Physiol.* **82**, 103–126 (2020).
10. Becker, H. M. & Deitmer, J. W. Proton transport in cancer cells: the role of carbonic anhydrases. *Int. J. Mol. Sci.* **22**, 3171 (2021).
11. Damaghi, M., Wojtkowiak, J. W. & Gillies, R. J. pH sensing and regulation in cancer. *Front. Physiol.* **4**, 370 (2013).
12. Justus, C. R. & Yang, L. V. GPR4 decreases B16F10 melanoma cell spreading and regulates focal adhesion dynamics through the G13/Rho signaling pathway. *Exp. Cell Res.* **334**, 100–113 (2015).
13. Justus, C. R. et al. Contextual tumor suppressor function of T cell death-associated gene 8 (TDAG8) in hematological malignancies. *J. Transl. Med.* **15**, 204 (2017).
14. Wang, H.-X. et al. Overexpression of G-protein-coupled receptors 65 in glioblastoma predicts poor patient prognosis. *Clin. Neurol. Neurosurg.* **164**, 132–137 (2018).
15. Ludwig, M. G. et al. Proton-sensing G-protein-coupled receptors. *Nature* **425**, 93–98 (2003).
16. Huang, X. P., Kenakin, T. P., Gu, S., Shoichet, B. K. & Roth, B. L. Differential roles of extracellular histidine residues of GPR68 for proton-sensing and allosteric modulation by divalent metal ions. *Biochemistry* **59**, 3594–3614 (2020).
17. Wang, J. Q. et al. TDAG8 is a proton-sensing and psychosine-sensitive G-protein-coupled receptor. *J. Biol. Chem.* **279**, 45626–45633 (2004).
18. Liu, J. P. et al. Each one of certain histidine residues in G-protein-coupled receptor GPR4 is critical for extracellular proton-induced stimulation of multiple G-protein-signaling pathways. *Pharm. Res.* **61**, 499–505 (2010).
19. Rowe, J. B., Kapolka, N. J., Taghon, G. J., Morgan, W. M. & Isom, D. G. The evolution and mechanism of GPCR proton sensing. *J. Biol. Chem.* **296**, 100167 (2021).
20. Duan, J. et al. Cryo-EM structure of an activated VIP1 receptor-G protein complex revealed by a NanoBIT tethering strategy. *Nat. Commun.* **11**, 4121 (2020).
21. Maeda, S. et al. Development of an antibody fragment that stabilizes GPCR/G-protein complexes. *Nat. Commun.* **9**, 3712 (2018).
22. Ballesteros, J. A. & Weinstein, H. In *Methods in Neurosciences*, Vol. 25 (ed. Stuart C. Sealfon) 366–428 (Academic Press, 1995).
23. Flock, T. et al. Universal allosteric mechanism for Galpha activation by GPCRs. *Nature* **524**, 173–179 (2015).
24. Wang, J. L. et al. Functional screening and rational design of compounds targeting GPR132 to treat diabetes. *Nat. Metab.* **5**, 1726–1746 (2023).
25. Nie, Y. et al. Specific binding of GPR174 by endogenous lysophosphatidylserine leads to high constitutive G(s) signaling. *Nat. Commun.* **14**, 5901 (2023).
26. Carpenter, B., Nehmé, R., Warne, T., Leslie, A. G. & Tate, C. G. Structure of the adenosine A(2A) receptor bound to an engineered G protein. *Nature* **536**, 104–107 (2016).
27. Ring, A. M. et al. Adrenaline-activated structure of  $\beta$ 2-adrenoceptor stabilized by an engineered nanobody. *Nature* **502**, 575–579 (2013).
28. Thom, C. et al. Structures of neurokinin 1 receptor in complex with G(q) and G(s) proteins reveal substance P binding mode and unique activation features. *Sci. Adv.* **7**, eabk2872 (2021).
29. Zhang, D. et al. Structural insights into angiotensin receptor signaling modulation by balanced and biased agonists. *EMBO J.* **42**, e112940 (2023).
30. Mochimaru, Y. et al. Extracellular acidification activates ovarian cancer G-protein-coupled receptor 1 and GPR4 homologs of zebra fish. *Biochem. Biophys. Res. Commun.* **457**, 493–499 (2015).
31. Katritch, V. et al. Allosteric sodium in class A GPCR signaling. *Trends Biochem. Sci.* **39**, 233–244 (2014).
32. Howard, M. K. et al. Molecular basis of proton-sensing by G protein-coupled receptors. *Cell* <https://doi.org/10.1016/j.cell.2024.11.036> (2024).
33. Isom, D. G., Cannon, B. R., Castaneda, C. A., Robinson, A. & Garcia-Moreno, B. High tolerance for ionizable residues in the hydrophobic interior of proteins. *Proc. Natl. Acad. Sci. USA* **105**, 17784–17788 (2008).
34. Luginina, A. et al. Structure-based mechanism of cysteinyl leukotriene receptor inhibition by antiasthmatic drugs. *Sci. Adv.* **5**, eaax2518 (2019).
35. Zhang, C. et al. High-resolution crystal structure of human protease-activated receptor 1. *Nature* **492**, 387–392 (2012).
36. Cheng, R. K. Y. et al. Structural insight into allosteric modulation of protease-activated receptor 2. *Nature* **545**, 112–115 (2017).
37. Wang, S. et al. D(4) dopamine receptor high-resolution structures enable the discovery of selective agonists. *Science* **358**, 381–386 (2017).
38. Rappas, M. et al. Comparison of orexin 1 and orexin 2 ligand binding modes using x-ray crystallography and computational analysis. *J. Med. Chem.* **63**, 1528–1543 (2020).
39. Fenalti, G. et al. Molecular control of  $\delta$ -opioid receptor signalling. *Nature* **506**, 191–196 (2014).
40. Zeghal, M., Laroche, G., Freitas, J. D., Wang, R. & Giguere, P. M. Profiling of basal and ligand-dependent GPCR activities by means of a polyvalent cell-based high-throughput platform. *Nat. Commun.* **14**, 3684 (2023).
41. Mashiko, M., Kurosawa, A., Tani, Y., Tsuji, T. & Takeda, S. GPR31 and GPR151 are activated under acidic conditions. *J. Biochem.* **166**, 317–322 (2019).
42. Guo, Y. et al. Identification of the orphan G protein-coupled receptor GPR31 as a receptor for 12-(S)-hydroxyeicosatetraenoic acid. *J. Biol. Chem.* **286**, 33832–33840 (2011).
43. Zhou, S. et al. Identification of 5 potential predictive biomarkers for Alzheimer's disease by integrating the unified test for molecular signatures and weighted gene coexpression network analysis. *J. Gerontol. A Biol. Sci. Med. Sci.* **78**, 653–658 (2023).
44. Haque, M. E. et al. The neuroprotective effects of GPR4 inhibition through the attenuation of caspase mediated apoptotic cell death in an MPTP induced mouse model of Parkinson's disease. *Int. J. Mol. Sci.* <https://doi.org/10.3390/ijms22094674> (2021).
45. Nehmé, R. et al. Mini-G proteins: Novel tools for studying GPCRs in their active conformation. *PLoS ONE* **12**, e0175642 (2017).
46. Punjani, A., Rubinstein, J. L., Fleet, D. J. & Brubaker, M. A. cryoSPARC: algorithms for rapid unsupervised cryo-EM structure determination. *Nat. Methods* **14**, 290–296 (2017).
47. Zheng, S. Q. et al. MotionCor2: anisotropic correction of beam-induced motion for improved cryo-electron microscopy. *Nat. Methods* **14**, 331–332 (2017).
48. Zhang, K. Gctf: Real-time CTF determination and correction. *J. Struct. Biol.* **193**, 1–12 (2016).
49. Jumper, J. et al. Highly accurate protein structure prediction with AlphaFold. *Nature* **596**, 583–589 (2021).

50. Varadi, M. et al. AlphaFold Protein Structure Database: massively expanding the structural coverage of protein-sequence space with high-accuracy models. *Nucleic Acids Res.* **50**, D439–d444 (2022).
51. Chen, Y. et al. Cryo-EM structure of the human adenosine A(2B) receptor-G(s) signaling complex. *Sci. Adv.* **8**, eadd3709 (2022).
52. Pettersen, E. F. et al. UCSF Chimera-a visualization system for exploratory research and analysis. *J. Comput. Chem.* **25**, 1605–1612 (2004).
53. Emsley, P., Lohkamp, B., Scott, W. G. & Cowtan, K. Features and development of Coot. *Acta Crystallogr. D. Biol. Crystallogr.* **66**, 486–501 (2010).
54. Adams, P. D. et al. PHENIX: a comprehensive Python-based system for macromolecular structure solution. *Acta Crystallogr. D. Biol. Crystallogr.* **66**, 213–221 (2010).
55. Sastry, G. M., Adzhigirey, M., Day, T., Annabhimoju, R. & Sherman, W. Protein and ligand preparation: parameters, protocols, and influence on virtual screening enrichments. *J. Comput. Aided Mol. Des.* **27**, 221–234 (2013).
56. Halgren, T. A. Identifying and characterizing binding sites and assessing druggability. *J. Chem. Inf. Model* **49**, 377–389 (2009).
57. Halgren, T. New method for fast and accurate binding-site identification and analysis. *Chem. Biol. Drug Des.* **69**, 146–148 (2007).

## Acknowledgements

This work was supported by the basic research program of the Science and Technology Commission of Shanghai Municipality (21JC1402400), the Fundamental Research Funds for the Central Universities (40500-20101-222383), and the National Natural Science Foundation of China grants 32171215 (G.S.), 82172644 (W.L.), 32371344 (H.R.), and 82230002 (M.L.). The authors thank the Instruments Sharing Platform of the School of Life Sciences, East China Normal University, and ECNU Multifunctional Platform for Innovation (O11). The authors thank Profs. Zhi-Jie Liu and Tian Hua for their guidance and assistance on EM sample preparation. The authors are grateful to the staff at the Core Facilities of Life Sciences Institute and the Center of Cryo-Electron Microscopy at Zhejiang University for their technical assistance.

## Author contributions

Yitong Ma optimized constructs, expressed and purified the complex proteins for cryo-EM studies, and edited the initial manuscript; Yijie Wang undertook the cAMP assays. Mengyuan Tang undertook cryo-EM data collection, 3D reconstruction and optimized the initial structure models. Yuan Weng helped cell culture and molecular cloning. Ying Chen and Yueming Xu assisted antibody and grid preparation. Shuxiao An did mutations for the cAMP assay. Yiran Wu and Suwen Zhao were involved in the model analysis and discussion. Huanhuan Xu and Dali Li

provided reagents and oversaw the data analysis, Mingyao Liu oversaw the project and edited the manuscript. Weiqiang Lu supervised the cAMP assay and edited the manuscript. Heng Ru supervised the cryo-EM data collection and structural modeling, and edited the manuscript. Gaojie Song supervised the project, analyzed the data, and wrote the manuscript.

## Competing interests

The authors declare no competing interests.

## Additional information

**Supplementary information** The online version contains supplementary material available at <https://doi.org/10.1038/s41467-025-55901-2>.

**Correspondence** and requests for materials should be addressed to Weiqiang Lu, Heng Ru or Gaojie Song.

**Peer review information** *Nature Communications* thanks Matthew Belousoff and the other, anonymous, reviewer(s) for their contribution to the peer review of this work. A peer review file is available.

**Reprints and permissions information** is available at <http://www.nature.com/reprints>

**Publisher's note** Springer Nature remains neutral with regard to jurisdictional claims in published maps and institutional affiliations.

**Open Access** This article is licensed under a Creative Commons Attribution-NonCommercial-NoDerivatives 4.0 International License, which permits any non-commercial use, sharing, distribution and reproduction in any medium or format, as long as you give appropriate credit to the original author(s) and the source, provide a link to the Creative Commons licence, and indicate if you modified the licensed material. You do not have permission under this licence to share adapted material derived from this article or parts of it. The images or other third party material in this article are included in the article's Creative Commons licence, unless indicated otherwise in a credit line to the material. If material is not included in the article's Creative Commons licence and your intended use is not permitted by statutory regulation or exceeds the permitted use, you will need to obtain permission directly from the copyright holder. To view a copy of this licence, visit <http://creativecommons.org/licenses/by-nc-nd/4.0/>.

© The Author(s) 2025